J|A|C|S ARTICLES

Published on Web 12/30/2010

Tuning the Structure and the Magnetic Properties of Metallo-supramolecular Polyelectrolyte−Amphiphile Complexes

Guntram Schwarz,*[,†,▽] Yves Bodenthin,[‡] Zbigniew Tomkowicz,[§,||] Wolfgang Haase,[§] Thomas Geue,[⊥] Joachim Kohlbrecher,[⊥] Ullrich Pietsch,[#] and Dirk G. Kurth[†,▽]

Julius-Maximilians University Würzburg, Chemical Technology of Advanced Materials, Röntgenring 11, D-97070 Würzburg, Germany, Swiss Light Source, Paul Scherrer Institute, CH-5232 Villigen-PSI, Switzerland, Institute of Physical Chemistry, Darmstadt University of Technology, Petersenstrasse 20, D-64287, Germany, Institute of Physics, Jagellonian University, Reymonta 4, 30-059 Kraków, Poland, Laboratory for Neutron Scattering, ETH Zurich and Paul Scherrer Institut, CH-5232 Villigen-PSI, Switzerland, University of Siegen, FB7 Solid State Physics, D-57068, Siegen, Germany, and Fraunhofer ISC, Neunerplatz 2, D-97082 Würzburg, Germany

Received September 17, 2010; E-mail: guntram.schwarz@matsyn.uni-wuerzburg.de

Abstract: Self-assembly of Fe^{2+} ions and the rigid ditopic ligand 1,4-bis(2,2′:6′,2″-terpyridin-4′-yl)benzene results in metallo-supramolecular coordination polyelectrolytes (MEPE). Sequential self-assembly of MEPE and dialkyl phosphoric acid esters of varying chain length via electrostatic interactions leads to the corresponding polyelectrolyte−amphiphile complexes (PAC), which have liquid−crystalline properties. The PACs have a stratified architecture where the MEPE is embedded in between the amphiphile layers. Upon heating above room temperature, the PACs show either a reversible or an irreversible spin-crossover (SCO) in a temperature range from 360 to 460 K depending on the architecture of the amphiphilic matrix. As the number of amphiphiles per metal ion is increased in the sequence 1:2, 1:4, and 1:6, the temperature of the SCO is shifted to higher values whereas the amphiphile chain length does not have a significant impact on the SCO temperature. In summary, we describe in this article how the structure and the magnetic response function of PACs can be tailored through the design of the ligand and the composition. To investigate the structure and the magnetic behavior, we use X-ray scattering, X-ray absorption spectroscopy, differential scanning calorimetry, faraday-balance, and superconducting quantum interference measurements in combination with molecular modeling.

Introduction

Spin transitions can occur in solids, liquid crystals, and complexes in solution and are generally molecular processes, driven by the entropy gain on going from the low-spin (LS) to the high-spin (HS) state.[1−5] The electronic properties of spin-transition compounds are affected by external stimuli, which make these materials potential candidates for scientific study and various applications alike.[6−8] The presence of two different stable electronic or magnetic states plays a central role for the development of storage media for signal processing[9] and transduction.[10] Temperature driven spin transitions are generally classified into a discontinuous type, in which the spin state conversion is accompanied by a thermal hysteresis and into a continuous type, where the conversion takes place without hysteresis. In many cases, the discontinuous type is accompanied by a structural change and can be well described by thermodynamics.[11] The structural phase transition is a consequence of

† Julius-Maximilians University Würzburg.
‡ Swiss Light Source, Paul Scherrer Institute.
§ Darmstadt University of Technology.
|| Jagellonian University.
⊥ Laboratory for Neutron Scattering, ETH Zurich and Paul Scherrer Institut.
University of Siegen.
▽ Fraunhofer ISC.

(1) Soyer, H.; Dupart, E.; Gómez-García, C. J.; Mingotaud, C.; Delhaès, P. *Adv. Mater. (Weinheim, Ger.)* **1999**, *11*, 382–384.
(2) Breuning, E.; Ruben, M.; Lehn, J.-M.; Renz, F.; Garcia, Y.; Ksenofontov, V.; Gütlich, P.; Wegelius, E.; Rissanen, K. *Angew. Chem., Int. Ed. Engl.* **2000**, *39*, 2504–2507.
(3) van Koningsbruggen, P. J.; Garcia, Y.; Kahn, O.; Fournès, L.; Kooijman, H.; Spek, A. L.; Haasnoot, J. G.; Moscovici, J.; Provost, K.; Michalowicz, A.; Renz, F.; Gütlich, P. *Inorg. Chem.* **2000**, *39*, 1891–1900.
(4) Galyametdinov, Y.; Ksenofontov, V.; Prosvirin, A.; Ovchinnikov, I.; Ivanova, G.; Gütlich, P.; Haase, W. *Angew. Chem., Int. Ed. Engl.* **2001**, *40*, 4269–4271.
(5) Gütlich, P.; Goodwin, H. A. *Spin Crossover in Transition Metal Compounds*; Springer: Berlin, Germany, 2004; Vol. 233, pp 234−235.
(6) Fujigaya, T.; Jiang, D. L.; Aida, T. *Chem. Asian J.* **2007**, *2*, 106–113.
(7) Forestier, T.; Mornet, S.; Daro, N.; Nishihara, T.; Mouri, S.-i.; Tanaka, K.; Fouche, O.; Freysz, E.; Letard, J.-F. *Chem. Commun.* **2008**, *432*, 7–4329.
(8) Volatron, F.; Catala, L.; Rivière, E.; Gloter, A.; Stéphan, O.; Mallah, T. *Inorg. Chem.* **2008**, *47*, 6584–6586.
(9) Lehn, J.-M. *Proc. Natl. Acad. Sci. U.S.A.* **2002**, *99*, 4763–4768.
(10) Kahn, O.; Martinez, C. J. *Science* **1998**, *279*, 44–48.
(11) Chernyshov, D.; Burgi, H.-B.; Hostettler, M.; Tornroos, K. W. *Phys. Rev. B* **2004**, *70*, 094116.

the spin transition, or both are coupled to each other.[12] Cooperative effects result in a thermal hysteresis and confer a memory effect on the system. Linear spin transition polymers with tightly coupled metal ions, such as Fe^{2+}−triazole complexes, have been proposed as a central design motif to control the cooperative switching in molecular magnetic materials.[10] Such compounds and other Fe^{2+} complexes have thus attracted considerable interest for developing functional materials with unique electronic and magnetic properties.[10,13] Coronado et al. recently applied the reverse micelle technique to fabricate bistable nanoparticles of polymeric $[Fe(Htrz)_2(trz)](BF_4)$.[14]

The concept of structure induced spin-crossover (SCO) was first demonstrated in Langmuir−Blodgett (LB) multilayers of polyelectrolyte−amphiphile complexes (PACs) self-assembled from 1,4-bis(2,2′:6′,2″-terpyridine-4′-yl)benzene, Fe^{2+} ions, and dihexadecyl phosphate (DHP) with a metal ion to DHP stoichiometry of 1:6. Langmuir−Blodgett transfers results in a PAC architecture where the amphiphilic molecules are arranged in double layers with opposing alkyl chains. The interstitial space is occupied by the rigid rodlike metallo-supramolecular polyelectrolyte (MEPE), which is formed through coordinative interaction between the terpyridine ligands and the Fe^{2+} ions.[15] Melting of the amphiphiles induces a reversible but partial SCO slightly above room temperature caused by a distortion of the coordination geometry around the central Fe^{2+} ions. Independently, Ruben and co-workers recently presented the spin transition in linear coordination polymers based on a ditopic bispyrazolylpyridine ligand.[16]

In an ideal octahedral ligand field, the transition metal 3d states split into degenerated t_{2g} (lower) and e_g (higher) levels. Any distortion of the coordination geometry, for example, as in the pseudo-octahedral geometry, leads to a further splitting, which implies that the effective energy separation between upper and lower sublevels is reduced. By taking this idea further, a distortion of the coordination geometry through an external stimulus can reduce the splitting of the 3d sublevels to such an extent that, at the given temperature, the spin state of the central metal ion changes from a low-spin to a high-spin state.[15] For this type of process, we favor to use the term spin crossover to draw a clear distinction to the well-established entropy driven spin transition phenomenon.

In contrast to LB layers, bulk PACs with an Fe^{2+} ion to amphiphile ratio of 1:2 show a nearly complete but irreversible SCO just above the melting temperature of the amphiphilic phase.[17,18] These PACs are prepared by precipitation from solution and can be described by alternating layers of interdigitated DHP and MEPE strata.[19] This material combines the liquid−crystalline properties through the amphiphile phase and SCO properties through the MEPE and constitutes therefore a new type of functional metallo-mesogen.[20]

In this work, we report how we can take advantage of the modularity of PACs to control the magnetic response function, including the temperature range, the reversibility, and the thermal hysteresis of the SCO. Basically, we can vary the ligand design, the metal ion, the amphiphilic chain length, and the metal ion to amphiphile ratio. Based on the MEPE assembled from Fe^{2+} and 1,4-bis(2,2′:6′,2″-terpyridin-4′-yl)benzene (**L1**),[21,22] the magnetic properties of the resulting Fe−PACs depend on the metal ion to amphiphile ratio, *R*, (1:2, 1:4, and 1:6) and the carbon chain length of the amphiphiles (C12, C14, and C16) as shown in the following. Considering the possible combinations, we count a total number of nine different PACs (Scheme 1 and Table 1). We demonstrate that the architecture and as a result the magnetic property of each PAC is different. To interrogate the structural changes and the magnetic properties, we utilize X-ray scattering (SAXS/WAXS), extended X-ray absorption fine structure (EXAFS) measurements, Faraday balance, and superconducting quantum interference (SQUID) measurement as well as differential scanning calorimetry (DSC), and molecular modeling. Finally, we compare the results of the PAC with a discrete metallocompound assembled from the flexible ligand 1,3-bis[4′-oxa(2,2′:6′,2″-terpyridinyl)]propane (reference).[21,22]

Results and Discussion

Preparation. The compounds are exclusively prepared by sequential self-assembly of metal ions, ligands, and amphiphiles. The composition of the final assembly is readily adjusted by choosing appropriate boundary conditions during self-assembly. It is of paramount importance for reproducible results to carefully control the stoichiometry of metal ions to ligands in MEPEs. Self-assembly of MEPE is performed under conductometric control as previously reported.[21,22] The PACs used in this study have metal ion to amphiphile ratios, *R*, of 1:2, 1:4, and 1:6. The amphiphiles are dialkyl phosphoric acid esters of varying chain lengths (C12: didodecyl-phosphate, DDP; C14: ditetradecyl-phosphate, DTP; and C16: dihexadecyl-phosphate, DHP). We use the following nomenclature: for example, Fe−PAC1_C16_1:4 specifies a PAC assembled from Fe^{2+}, ligand **L1**, DHP (C16), and a metal ion to amphiphile ratio of 1:4; unless otherwise mentioned, we use the simplified nomenclature PAC_C16_1:4 because the bulk of the results refer to the PAC prepared with Fe^{2+} and ligand **L1**.

Structure Characterization of PAC at Ambient Conditions. As a representative example, we focus in the following on the detailed analysis of PAC_C16_1:4. First, we discuss the alkyl chain packing within the amphiphilic matrix. Figure 1 shows the measured wide-angle scattering intensity (*I*) (circles) as a function of the transfer momentum (q) in the range between $1\ Å^{-1} < q < 2\ Å^{-1}$ as well as simulated spectra (red curves). Beside a main peak at $q = 1.52\ Å^{-1}$, we note four additional signals. In the case of hexagonal packing of all-trans alkyl chains, a peak at $q = 1.52\ Å^{-1}$ is expected (Figure 1 middle,

(12) Jeftic, J.; Romstedt, H.; Hauser, A. *J. Phys. Chem. Solids* **1996**, *57*, 1743–1750.
(13) Halder, G. J.; Kepert, C. J.; Moubaraki, B.; Murray, K. S.; Cashion, J. D. *Science* **2002**, *298*, 1762–1765.
(14) Coronado, E.; Galán-Mascarós, J. R.; Monrabal-Capilla, M.; García-Martínez, J.; Pardo-Ibáñez, P. *Adv. Mater.* **2007**, *19*, 1359–1361.
(15) Bodenthin, Y.; Pietsch, U.; Möhwald, H.; Kurth, D. G. *J. Am. Chem. Soc.* **2005**, *127*, 3110–3114.
(16) Rajadurai, C.; Fuhr, O.; Kruk, R.; Ghafari, M.; Hahn, H.; Ruben, M. *Chem. Commun.* **2007**, 2636–2638.
(17) Bodenthin, Y.; Schwarz, G.; Tomkowicz, Z.; Nefedov, A.; Lommel, M.; Mohwald, H.; Haase, W.; Kurth, D. G.; Pietsch, U. *Phys. Rev. B* **2007**, *76*, 064422−064426.
(18) Bodenthin, Y.; Schwarz, G.; Tomkowicz, Z.; Geue, T.; Haase, W.; Pietsch, U.; Kurth, D. G. *J. Am. Chem. Soc.* **2009**, *13*, 2934–2941.
(19) Meister, A.; Förster, G.; Thünemann, A. F.; Kurth, D. G. *ChemPhysChem* **2003**, *4*, 1095–1100.
(20) Seredyuk, M.; Gaspar, A. B.; Ksenofontov, V.; Galyametdinov, Y.; Kusz, J.; Gütlich, P. *J. Am. Chem. Soc.* **2008**, *130*, 1431–1439.
(21) Schwarz, G.; Bodenthin, Y.; Geue, T.; Koetz, J.; Kurth, D. G. *Macromolecules* **2010**, *43*, 494–500.
(22) Schwarz, G.; Sievers, T. K.; Bodenthin, Y.; Hasslauer, I.; Geue, T.; Koetz, J.; Kurth, D. G. *J. Mater. Chem.* **2010**, *20*, 4142–4148.

Scheme 1. Sequential Self-Assembly of Fe^{2+} Ions and 1,4-Bis(2,2′:6′,2″-terpyridine-4′-yl)benzene (**L1**) Results in Metallo-supramolecular Polyelectrolytes (MEPEs)[a]

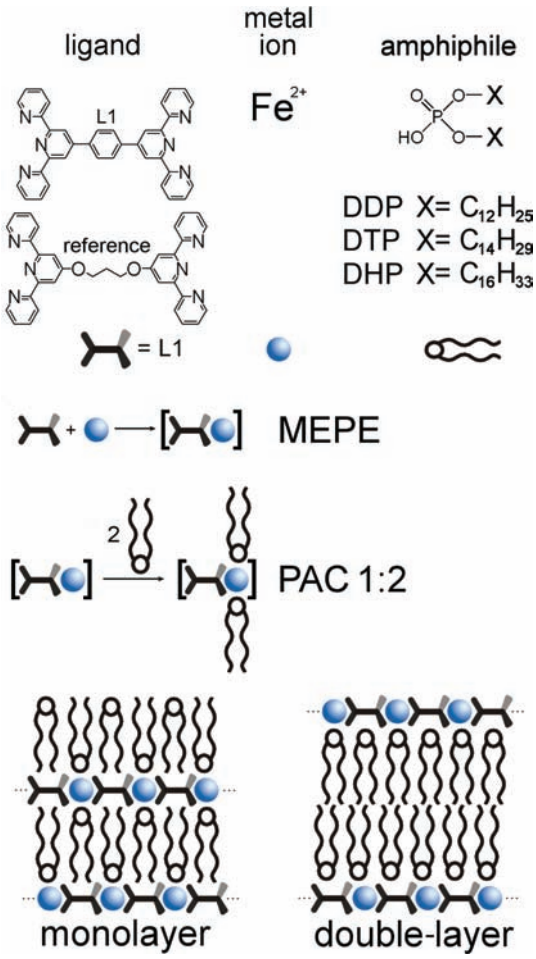

[a] The octahedral coordination geometry in the MEPE chain is indicated by the wedges. The exchange of the acetate ions (not shown) by amphiphiles gives rise to a polyelectrolyt amphiphile complex (PAC). The ratio of metal ion to amphiphiles, *R*, is adjustable through the experimental conditions. The MEPE chains are embedded in the interstitial space between amphiphile layers. Depending on *R* and the chain length, different layer structures are preferred. For $R = 1{:}2$ (schematic shown) and 1:6, monolayer structures with interdigitating amphiphiles predominate, and the layer sequence is MEPE/amphiphiles. For $R = 1{:}4$, double layer structures predominate with the sequence MEPEs/amphiphiles/amphiphiles. Metal ion induced self-assembly of the reference ligand results in ring-shaped metallo-oligomer species, and the above mentioned exchange of the counter ions gives rise to oligomer amphiphilic complexes (OAC) with amphiphilic structures similar to the PAC.

asterisk marked).[23] For a single undistorted hexagonal packing mode, only one reflection peak is observable because the (100) and (010) reflections coincide. Therefore, the observed peak corresponds to the previously published two-dimensional orthorhombic methylene subcell (SC) with a width of $a_{SC} = 4.75$ Å, a height $b_{SC} = 8.23$ Å, an angle $\alpha_{SC} = \beta_{SC} = \gamma_{SC} = 90°$, and a next neighbor periodicity of 4.1 Å, corresponding to the alkyl chain diameter.[19,23] The setting angle, τ, between the carbon backbone of the subcell and a_{SC} is 59.2°. The additional peaks shown in the left and right scattering curve of Figure 1 reveal that, besides hexagonal packing (Figure 1 middle), also other packing motives are present in the PAC. In the left scattering

(23) Förster, G.; Meister, A.; Blume, A. *Curr. Opin. Colloid Interface Sci.* **2001**, *6*, 294–302.

Table 1. WAXS Peak Positions and Dimensions of the Methylene Subcells of All Samples in the Range of $1\ Å^{-1} \le q \le 2\ Å^{-1}$[a]

	WAXS reflexes ($Å^{-1}$)	methylene subcell			alkyl chain
sample name	$1\ Å^{-1} \le q \le 2\ Å^{-1}$	a_{SC} (Å)	b_{SC} (Å)	τ (°)	base area ($Å^2$)
PAC_C12_1:2	1.44[b]	–	–	–	–
PAC_C12_1:4	1.48; 1.57; 1.75	5.01	7.93	61	20.1
PAC_C12_1:6	1.48; 1.56; 1.74	5.01	7.93	61	20.1
PAC_C14_1:2	1.53[b]	–	–	–	–
PAC_C14_1:4	1.49; 1.65; 1.77	4.51	8.19	62.1	19.1
PAC_C14_1:6	1.49; 1.65; 1.77	4.51	8.19	62.1	19.1
PAC_C16_1:2	1.51	4.81	8.32	60	20
PAC_C16_1:4	1.32; 1.39; 1.5; 1.52	4.14	9.08	66.2	18.8
	1.5; 1.52; 1.68	5.06	7.43	66.0	18.8
PAC_C16_1:6	1.3; 1.39; 1.5; 1.52	4.1	9.02	65.9	18.5
	1.5; 1.52; 1.67	5.05	7.43	66.0	18.8
OAC_C16_1:6	1.52	4.75	8.23	59.2	19.5

[a] Dimensions of methylene subcells (a_{SC}, b_{SC}, τ) for simulation of alkyl chain packing as described in the text. [b] Peak too broad for assignment.

curve of Figure 1, besides the main peak at $q = 1.52\ Å^{-1}$ marked with an asterisk, we observe reflections at $q = 1.32\ Å^{-1}$ and $q = 1.39\ Å^{-1}$ as well as the shoulder at $q = 1.50\ Å^{-1}$, which are best simulated by elongated hexagonal subcells with $a_{SC} = 4.14$ Å, $b_{SC} = 9.08$ Å, and $\tau = 66.2°$. Likewise, the shoulder at $1.50\ Å^{-1}$ together with the signal at $q = 1.68\ Å^{-1}$ can be simulated by a compressed hexagonal subcell with dimensions of $a_{SC} = 5.06$ Å, $b_{SC} = 7.43$ Å, and $\tau = 66°$ (right scattering curve). On the basis of these subcells, we model discrete DHP double layers and simulate powder spectra for both cell types as shown in Figure 1 (red lines left and right). The simulated powder spectra are in agreement with the calculated subcell reflexes. Table 1 collects the measured WAXS reflexes from all nine PACs and the flexible metallo-oligomer based reference compound, OAC, (Scheme 1), the values of the calculated methylene subcells, and the size of the alkyl chain base areas.

Figure 2 shows the experimental (gray circles) and the simulated (red line) small-angle scattering intensity (I) as a function of the transfer momentum (q). The angle dispersive scattering experiment was performed in the range of $0.05\ Å^{-1} \le q \le 0.8\ Å^{-1}$. The experimental scattering curve exhibits three equidistant peaks at $q_{hk1} = 0.12\ Å^{-1}$, $q_{hk2} = 0.24\ Å^{-1}$, and $q_{hk3} = 0.36\ Å^{-1}$ according to the Bragg reflexes from the first to the third order and a periodicity (d_{DL}) of 51.9 ± 0.5 Å (Figure 2: stars). The average thickness of a MEPE rod is approximately 9 Å, and the length of a fully extended all-trans DHP molecule is 23 Å. If we assume that DHP and MEPE are associated by electrostatic interactions, we propose that the signals originate from lamellae composed of DHP/MEPE/DHP strata. In the following, we refer to this architecture as double layer (DL). A fourth order reflex is very weak but existent therefore indicating long-range order in the lamella direction. From the full-width-at-the-half-maximum of the first order peak, a correlation length of 312 Å is calculated, which is equivalent to the length of approximately six double layers. The peaks at $q = 0.189\ Å^{-1}$, $q = 0.38\ Å^{-1}$, and $q = 0.57\ Å^{-1}$ correspond to a periodicity of (d_{ML}) 33.3 Å. With the same arguments as above, we conclude that this set of signals belongs to a lamella with the sequence MEPE/DHP, which is referred to a monolayer (ML) in the following (Figure 2: diamonds). In order to preserve electroneutrality, the DHP monolayer is assumed to be interdigitated.[18,19] We estimate the correlation length to be 436 Å equivalent to approximately 13 consecutive monolayers. We conclude that two lamella motives, namely, the ML and the DL architecture, coexist in the sample. The DL structure is predominating as a

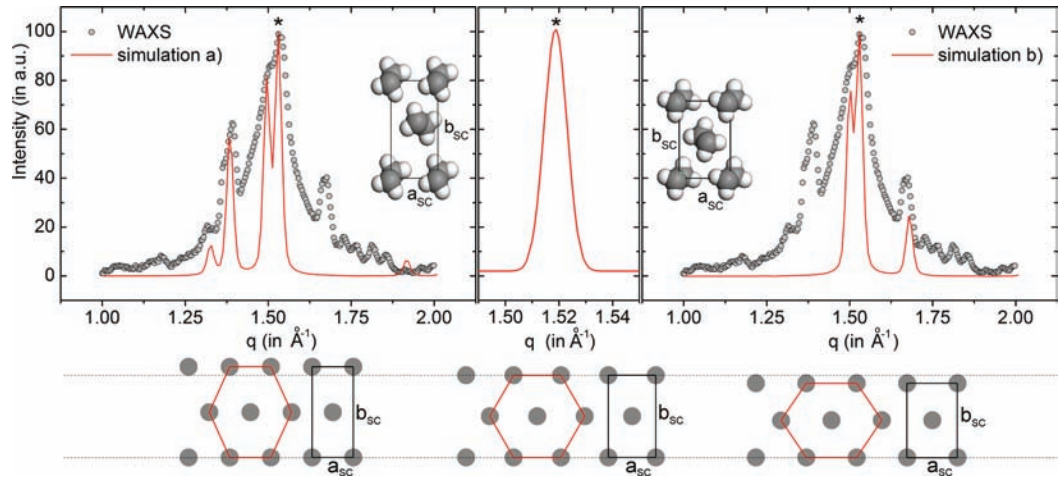

Figure 1. (Top) Experimental (circles) and simulated (red lines) wide-angle X-ray scattering intensities (I) of PAC_C16_1:4 as a function of transfer momentum (q). The entire PAC architecture composed of MEPE and DHP is used for the simulation of the scattering data as described in the text. The amphiphilic phase is composed of three packing motives. The main reflex at $q = 1.52$ Å^{-1} (asterisk) is assigned to hexagonally packed methylene chains forming a subcell with dimensions of $a_{SC} = 4.75$ Å and $b_{SC} = 8.23$ Å. The other peaks are assigned to an elongated (right) and a compressed (left) subcell (inset); see text for details. (Bottom) Schematic showing the alkyl chain packing in the amphiphilic layer.

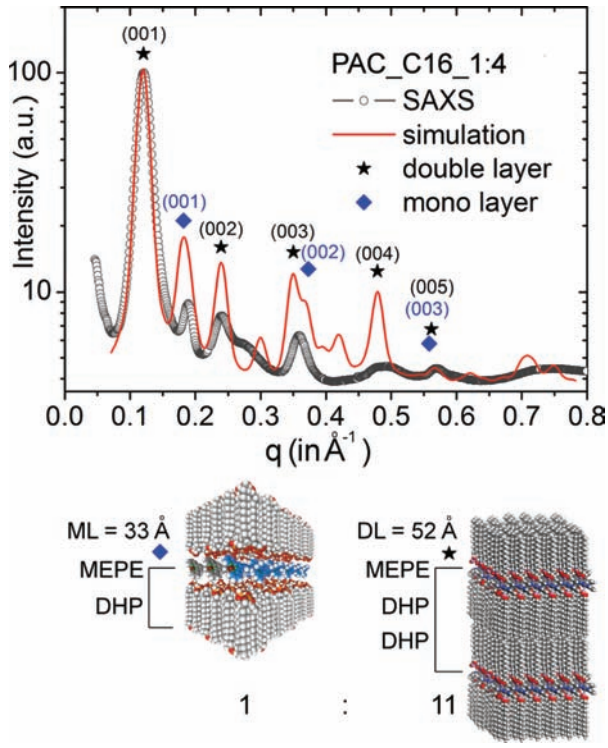

Figure 2. (Top) Experimentally determined (gray circles) and simulated (red line) scattering intensity (I) as function of transfer momentum (q) of PAC_C16_1:4. In this sample, two packing motives coexist. The amphiphiles can form an interdigitaded monolayer with a thickness of 33 Å and a noninterdigitated DHP double layers with $d = 52$ Å. (Bottom) Image of a modeled ML supercell (left) and a DL supercell (right). The asterisks and the diamonds mark the Bragg reflex positions caused by the DL and ML cells, respectively.

comparison of the intensities of the DL and ML first order peaks reveals. The DL scattering peak has a 28-fold stronger intensity than the ML scattering peak. In summary, we note that the scattering data reveals different packing motives in the alkyl chain packing as well as in the lamellar organization of the components.

We are now in a position to refine the complete architecture at all length scales of the PAC by computer modeling of the

Table 2. List of the Measured First Order SAXS Reflexes (q) for the Mono- (ML) and Double Layers (DL) of PAC and OAC, the Experimental Determined Layer Thicknesses (d), and the DL to ML Ratios as well as the Theoretical Layer Thickness (d_{th}) Based on All-Trans Straight Alkyl Chains of the Amphiphiles

	q_{DL} (Å^{-1})	d_{DL}/ d_{th} (Å)	q_{ML} (Å^{-1})	d_{ML}/ d_{th} (Å) (d_i)	DL/ML ratio
PAC					
C12_1:2	Broad peak from $q = 0.148$ Å^{-1} to 0.233 Å^{-1}				
C12_1:4	0.148	42.5/46.3	0.241	26.1/28.3	9.3
C12_1:6	0.148	42.5/46.3	0.241	26.1/28.3	2.8
C14_1:2	Broad peak from $q = 0.137$ Å^{-1} to 0.208 Å^{-1}				
C14_1:4	0.134	46.8/51.3	0.210	29.9/30.8	8.2
C14_1:6	0.134	46.8/51.3	0.210	29.9/30.8	1.7
C16_1:2	−	−	0.196	32.1	0:1
C16_1:4	0.121	51.9/56.3	0.189	33.3/33.3	8.1
C16_1:6	0.121	51.9/56.3	0.189	33.3/33.3	0.3
OAC					
C16_R1:4	0.121	51.9/56.3	0.189	33.3/33.3	3.9
C16_R1:6	0.121	51.9/56.3	0.189	33.3/33.3	0.2

structure and the scattering intensities until we obtain a best match of experimental and simulated data. To simulate the PAC_C16_1:4 small angle scattering curve, we construct a superunit containing a DHP double layer according to the above-mentioned methylene subcell (Table 1) and a $Fe_2(\mathbf{L1})_2$ repeat unit representing the MEPE component. The energy is minimized without restrictions. The final model consists of a $3 \times 2 \times 2$ supercell with the dimension of 48 Å × 67 Å × 105 Å assembled from 11 DL superunits and 1 ML superunit. The latter one has interdigitated DHP molecules as described in the literature.[19] As mentioned above, the sample consists to approximately 97% of DL structure. To keep the supercell small, the simulation is performed with a DL fraction of approximately 91%, and as a result, the simulated intensity of the ML first order peak in Figure 2 is higher than the intensity of the experimental scattering peak. The experimental and the simulated scattering curves were normalized to 100 on the basis of the highest intensities at $q = 0.12$ or the first order DL Bragg reflex. Table 2 summarizes the scattering data of all samples.

Next, we take a detailed look at the energy-minimized PAC_C16_1:4 model. The DHP molecules are oriented with the alkyl chains perpendicular to the MEPE chains, and the interstitial space between the amphiphile layers has a thickness

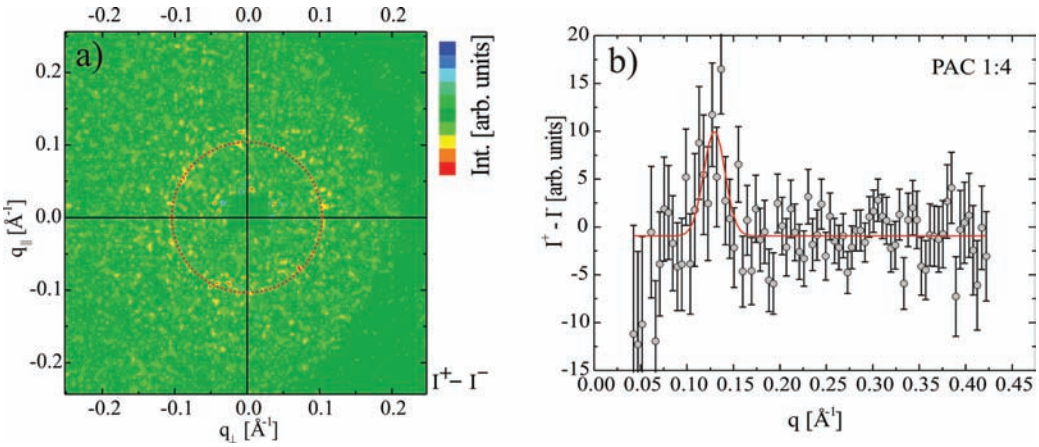

Figure 3. (a) Color-coded azimuthal average of the intensity differences $I^+ - I^-$ of polarized small-angle neutron scattering as a function of the transfer momentum (q) of PAC_C16_1:4 pictured in 2D. The weak ring at $q = 0.12$ Å^{-1} coincides with the position of the Bragg peak of the characteristic double lamella structure. The dotted circle is added to guide the eye. (b) Gray circles show $I^+ - I^-$ as a function of q. A weak surplus of spin up neutron scattering intensity is visible at $q = 0.12$ Å^{-1} accentuated through the red fit.

of 10.3 Å. In the ML structure, the DHP molecules are in a straight all-trans configuration, and the thickness of the interdigitated DHP monolayer is 23 Å, which corresponds very well with the effective length of that molecule.[24] However, in the DL structure, the DHP thickness is 20.7 Å, and the overall length is shortened by approximately 2.3 Å. Defects in alkyl chains, such as end-gauche, gauche−gauche and gauche−trans−gauche kink conformations, are well-known and result in an reduced effective length.[25,26] Using infrared spectroscopy, we observe a shift of the CH_2 C−H stretching modes from 2919 and 2851 cm^{-1} to 2918 and 2848 cm^{-1} indicating the existence of defects in an all-trans crystalline conformation of the alkyl chains.[27,28] The energy-minimized PACs show slightly bent alkyl chains. Therefore, we conclude that defects in the amphiphilic layer reduce the overall thickness. As a result, the calculated thickness of d_{DL} is 52 Å and d_{ML} is 33 Å, respectively, which is in excellent agreement with the experimental SAXS data of $d_{DL} = 51.9 \pm 0.5$ Å and $d_{ML} = 33.3 \pm 0.5$ Å (Table 2).

Small-angle neutron scattering (SANS) is performed to confirm the obtained SAXS data. Through three different sample−detector geometries, we are able to cover a q range of 0.001 Å$^{-1} \le q \le 0.388$ Å^{-1}. For PAC_C16_1:4, we could verify that the Bragg reflection at $q = 0.12$ Å^{-1} (DL) is the reflection with the lowest observable periodic q value, confirming that the predominant superstructure for this PAC is the double-layer structure. To obtain further information on structure and magnetism, we carried out polarized SANS. An applied magnetic field of $B = 11$ T aligns the magnetic moment of the sample. The magnetic field vector stands perpendicular to the incident polarized neutron beam, and the neutron spins are aligned either antiparallel (+) or parallel (−) to the field. The spin polarization of the scattered neutrons is not analyzed because spin reversion (flip) events are not accounted for.[29] For polarized neutrons (+ or −), the scattering intensities $I^+(q, \alpha)$ and $I^-(q, \alpha)$ are different (α is the angle between the magnetic moment of the sample and the scattering vector). This difference is proportional to the magnetic−nuclear cross term, $I^+(q, \alpha) - I^-(q, \alpha) \propto 2F_N F_M \sin^2\alpha$ where F_N represent the nuclear and F_M the magnetic scattering form factors.[29] F_N is independent from the scattering angle and the magnetic moment of the neutrons. The intensity difference is based on the resulting magnetic moment of the sample and the magnetic interaction with the polarized neutrons. Azimuthal integration of the whole 2D scattering intensity pattern leads to $I^+(q) - I^-(q) \propto F_N F_M$ and yields even for small magnetic contributions to a measurable signal. In the polarized neutron scattering experiment, the first order Bragg peak for the double layer in PAC appears at the same position ($q \sim 0.12$ Å^{-1}) as observed for unpolarized SANS and SAXS experiments and is in the case of a high-spin Fe−MEPE strata caused by both nuclear and magnetic origin. Figure 3 shows the intensity difference $I^+(q) - I^-(q)$ between spin up (+) and spin down (−) polarized neutrons as a function of q. After an azimuthal average of the scattering pattern, a weak excess of spin up polarized neutrons is observed at $q = 0.12$ Å^{-1} proving the presence of magnetic moments, which can only be localized in the iron ions of MEPE, in a layer with a periodicity of $d \sim 52$ Å.

Next, we discuss results from PAC_C12 and PAC_C14. The lengths of all-trans DDP and DTP molecules are 18 and 20.5 Å, respectively, and therefore, the thicknesses of the interdigitated monolayers are expected to be 28.3 and 30.8 Å, respectively. The simulations for $R = 1{:}6$ afford 26.4 and 30.1 Å in agreement with the experimental data of $d_{ML} = 26.1 \pm 0.5$ Å for DTP and $d_{ML} = 29.9 \pm 0.5$ Å for DDP. In the simulations, the alkyl chains are in a first approximation in an all-trans configuration; however, upon close inspection, they also show a slight bending, which accounts for the reduced thickness. For a PAC double layer, we theoretically expect thicknesses of 46.3 and 51.3 Å in the case of DDP and DTP, respectively. From the simulations for $R = 1{:}4$, we determine 42.7 and 47 Å for d_{DL}, which again agrees with the scattering data ($d_{ML} = 42.5 \pm 0.5$ Å for DTP and $d_{ML} = 46.8 \pm 0.5$ Å for DDP).

We conclude that, for longer alkyl chains (≥C16) and R ≥ 1:4, the amphiphiles are straight while for shorter chains or lower stoichiometries the layer thickness is somewhat smaller than expected for straight all-trans alkyl chains (Table 2). Most likely

(24) Kitaigorodkij, A. I. *Organic Chemical Crystallography*; Consultants Bureau: New York, 1961.
(25) Dorset, D. L.; Moss, B.; Wittmann, J. C.; Lotz, B. *Proc. Natl. Acad. Sci. U.S.A.* **1984**, *81*, 1913–1917.
(26) Laibinis, P. E.; Whitesides, G. M.; Allara, D. L.; Tao, Y. T.; Parikh, A. N.; Nuzzo, R. G. *J. Am. Chem. Soc.* **1991**, *113*, 7152–7167.
(27) Snyder, R. G.; Maroncelli, M.; Qi, S. P.; Strauss, H. L. *Science* **1981**, *214*, 188–190.
(28) Nuzzo, R. G.; Dubois, L. H.; Allara, D. L. *J. Am. Chem. Soc.* **1990**, *112*, 558–569.
(29) Wiedenmann, A. *Phys. B (Amsterdam, Neth.)* **2001**, *297*, 226–233.

this is not due to gauche defects but to a slight bending of the alkyl chains caused by packing effects as indicated by molecular modeling. Also, we notice that the DL to ML ratios in the PAC series change from 0.3 to 9.3 (Table 2) whereas this value for the same PAC varies not more than ±10% (±0.9) from sample to sample.

In summary, we can make three important conclusions from scattering data and molecular modeling. Within a PAC, we find different structure motives at different length scales. At the molecular level, the alkyl chains are packed in a hexagonal or distorted hexagonal lattice. Only in PAC_C16_1:2 the alkyl chains are packed in perfectly hexagonal lattice. In the other PACs, we find the presence of several packing motives, namely, hexagonal and distorted hexagonal, depending on alkyl chain length and stochiometry. At the supramolecular length scale, domains with amphiphilic mono- and double layers can coexist in PACs. The exception is again PAC_C16_1:2, which contains only the interdigitated ML motive. The SAXS data of PAC_C12_1:2 and PAC_C14_1:2 show neither a distinct monolayer nor a double layer peak (Table 2 and Figure S1 of the Supporting Information). For all PACs with $R = 1{:}4$, the double layer is the predominant structure motive. In PAC_C16_1:4, the magnetic layer has a periodicity of $d \sim 52$ Å proving the sequence MEPE/DHP/DHP for the double-layer motive. Finally, we note that PACs, which differ only in the central metal ion (Fe(II), Co(II), Ni(II), or Zn(II)), show identical SAXS and WAXS curves (Figure S2 of the Supporting Information).

Magnetic Properties of PAC. Magnetic measurements are performed on a Faraday balance in a temperature range 273−470 K and a SQUID in the range from 2 to 393 K, respectively, as described in the Experimental Section. The SQUID data follows the Curie−Weiss law and is consistent with the background corrected Faraday balance data proofing the accuracy of the measurements as shown in Figure S3 of the Supporting Information for PAC_C16_1:6. In the following, the data is presented in $\chi_M T$, the product of magnetic susceptibility and temperature.

In Figure 4, we present $\chi_M T$ of the PAC series as function of temperature. At ambient conditions, the samples are not purely diamagnetic. Varying amounts of defects in the MEPE chain result in a HS fraction of Fe^{2+} ions from 10 to 25%.[17,18] In the present PAC series, we find that the magnetic susceptibility differs from $\chi_M T = 0.03{-}0.21$ cm^3 mol^{-1} K or in terms of effective magnetic moment between 0.5 and 1.3 μB/Fe^{2+}. As one can see, for all samples, the magnetic moment that is the fraction of HS−Fe^{2+} increases with temperature indicating spin-crossover. Assuming pure spin magnetism, the magnetic moment of free HS−Fe^{2+} is estimated to be 3.0 cm^3 mol^{-1} K or 4.9 μB/Fe^{2+}. On this basis, the average spin-crossover temperature (T_{aSCO}) is determined (Figure 3, arrows) at $\chi_M T = 0.75$ cm^3 mol^{-1} K (2.45 μB/Fe^{2+}) where half of the Fe^{2+} ions are in the HS state (Figure 4, dotted line). This value can be considered as a lower limit, for example, Constable et al. determined a $\chi_M T$ value of up to 0.88 cm^3 mol^{-1} K for mononuclear $[Fe(tpy)_2]^{2+}$ complexes ($g = 2.16$) where half of the Fe^{2+} ions are in the HS state.[30]

As shown in Table 3, T_{aSCO} significantly shifts to higher values as the fraction of amphiphiles in PAC increases. The amphiphile chain length, on the other side, does not significantly effect T_{aSCO}. PACs with $R = 1{:}4$ undergo a nearly complete but partially reversible SCO (Figure 4). After heating to 430 K, the HS−Fe^{2+} fraction increases from 11.6, 12.2, and 10.2% to 89.4, 83.3, and 84.7% for C12, C14, and C16, respectively. After cooling to room temperature, the values decrease to 48.3, 38.4, and 44.2% according to magnetic susceptibilities of $\chi_M T = 0.7$, 0.44, and 0.59 cm^3 mol^{-1} K.

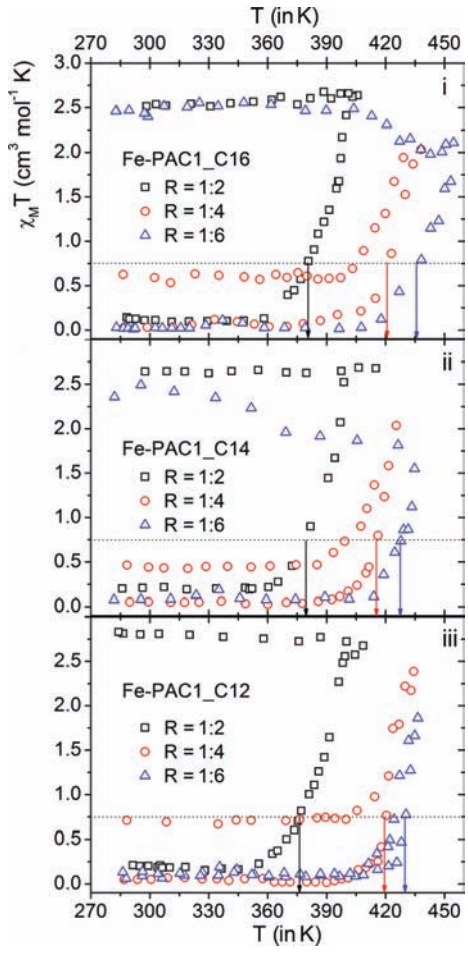

Figure 4. Product of magnetic susceptibility (χ_M) and temperature (T) as a function of temperature (T) of different Fe−PACs during a first heating−cooling cycle. The increase of $\chi_M T$ during heating indicates a spin-crossover between a diamagnetic low-spin and a paramagnetic high-spin state of the Fe^{2+} ions. The average spin-crossover temperature (arrows) depends mainly on the metal ion to amphiphile ratio (1:2, black squares; 1:4, red circles; and 1:6, blue triangles). The amphiphilic chain length of the PACs (i, C12; ii, C14; and iii, C16) does not affect the spin-crossover temperature significantly. Depending on the metal ion to amphiphile ratio, the SCO is irreversible ($R = 1{:}2$, black squares), partially reversible ($R = 1{:}4$, red circles), or totally reversible ($R = 1{:}6$, iii, blue triangles).

Table 3. Onset and Average Spin-Crossover Temperature (T_{oSCO}/T_{aSCO} (in Kelvin)) of the PAC Series Determined with a Faraday Balance and a SQUID (error ±2 K)[a]

	C12	C14	C16
Fe−PAC1	T_{oSCO}/T_{aSCO}	T_{oSCO}/T_{aSCO}	T_{oSCO}/T_{aSCO}
$R = 1{:}2$	355/376 (i, ML)	360/378 (i, ML)	362/380 (i, ML)
$R = 1{:}4$	398/420 (r*, DL)	396/416 (r*, DL)	392/421 (r*, DL)
$R = 1{:}6$	410/429 (r, DL)	413/428 (i, ML)	412/436 (i, ML)

[a] i: Irreversible complete SCO; r*: partially reversible; r: reversible; ML: predominantly monolayer architecture in PAC; DL: predominantly double layer architecture in PAC.

(30) Constable, E. C.; Baum, G.; Bill, E.; Dyson, R.; Eldik, R. v.; Fenske, D.; Kaderli, S.; Morris, D.; Neubrand, A.; Neuburger, M.; Smith, D. R.; Wieghardt, K.; Zehnder, M.; Zuberbühler, A. D. *Chem.—Eur. J.* **1999**, *5*, 498–508.

For PAC_C12_1:6 $\chi_M T$ is 0.06 $cm^3\ mol^{-1}\ K$ at room temperature and increases after heating to 435 K to $\chi_M T = 3.9$ $cm^3\ mol^{-1}\ K$ equivalent to a 80% HS−Fe^{2+}. Cooling the sample back down to room temperature results in a decrease of $\chi_M T$ to 0.12 $cm^3\ mol^{-1}\ K$, which means that the SCO is almost completely reversible. We have not so far observed complete reversibility for any other examined PAC system. Additionally, we note that, before heating, the double layer structure dominates the architecture in PACs with R = 1:4 and in PAC_C12_1:6 (Table 2).

In PAC_C16_1:2 as well as in PAC_C16_1:6 and PAC_C14_1:6, the amphiphiles are predominantly organized in the monolayer structure. In these cases, the SCO is irreversible. Upon heating of PACs with R = 1:2 $\chi_M T$ increases up to ≥2.65 $cm^3\ mol^{-1}\ K$ and remains constant from 405 to 435 K and upon cooling down to room temperature. Thermogravimetric analysis of PACs shows no mass loss due to decomposition up to 463 K, and therefore, we chose 453 K as the upper temperature limit for the measurements.

For PAC_C14_1:6 and PAC_C16_1:6, the increase of $\chi_M T$ does not stop immediately with cooling indicating a nonequilibrium situation where the HS−state has not yet completely developed before cooling has started. Hence, $\chi_M T$ increases further from 1.8 to 2.5 $cm^3\ mol^{-1}\ K$ for PAC_C14_1:6 and from 2.1 to 2.5 $cm^3\ mol^{-1}\ K$ for PAC_C16_1:6, respectively.

In PAC Langmuir−Blodgett films, melting of the amphiphilic matrix causes a reversible but partial spin-crossover slightly above room temperature.[15,31] The magnetic moment increases by about 0.54 $\mu B/Fe^{2+}$. We observe a similar behavior for bulk PAC with R = 1:6 and PAC_C16_1:4 in a temperature range of 313−343 K (Figure 4i). The magnetic susceptibility increases reversibly up to 0.22 $cm^3\ mol^{-1}\ K$ or 0.55 $\mu B/Fe^{2+}$ if the temperature does not exceed 345 K. Interestingly, $\chi_M T$ decreases again above 345 K until at approximately 400 K the spin-crossover occurs. Currently, we do not have an explanation for this behavior. Presumably, melting of the amphiphilic matrix initially causes more defects and a rise in $\chi_M T$. As the matrix becomes more fluid, the MEPE may anneal driven by the metal ion ligand interaction thus reducing the number of HS−Fe^{2+} sites along the backbone of the assembly. As a result, $\chi_M T$ decreases again.

In summary, all characterized Fe−PAC1 show a spin-crossover in the temperature range from 350 to 460 K. For PACs with predominant double layer architecture, the SCO is nearly complete and partially or totally reversible after cooling to room temperature. In contrast, all PACs with mainly monolayer packing motive develop into a frozen HS state. The SCO temperature (T_{oSCO}) increases with the metal to amphiphile ratio but not significantly with the amphiphilic chain length.

Temperature Dependent Structure Characterization of PAC. Next, we are going to address the question how the temperature dependent changes of the PAC architecture influence the magnetic properties, which are the spin-crossover temperatures T_{oSCO} (onset) and T_{aSCO} (average), the degree of reversibility, as well as the magnitude of the magnetic response. Therefore, we will present data of the temperature dependent architecture of the amphiphile matrix using differential scanning calorimetry and temperature dependent SAXS and WAXS measurements. In the following sections, we will focus on PAC_C16_1:6 as an example for a PAC with a monolayer packing motive and an irreversible SCO. These results will be compared to PAC_C16_1:4 and PAC_C12_1:6 with a double layer packing motive and partially or totally reversible SCO. The enthalpy during phase-, spin- or structure transitions can be determined by differential calorimetery. We measure the heat flow (q_f) or the specific heat (c_p) as a function of temperature. Figure 5i shows c_p of PAC_C16_1:6 during heating in a temperature range of 273−473 K. In total, we observe four regions (**A**−**D**) related to different transitions. Transition **A** from 305 to 327 K (Figure 5) corresponds to the decrease of the long-range order of the lamella. In this range, we note a loss of scattering intensity of the monolayer Bragg reflexes (Figure 6i) whereas the related ML thickness remains approximately constant at $d = 33.3 \pm 0.5$ Å. The constant WAXS intensity in this temperature region indicates that the alkyl chain packing is not affected up to a temperature of 331 K (Figure 6iv). Above this temperature (region **B**), the amphiphiles start to melt as indicated by a decrease of the WAXS intensity (Figure 6v). Further heating leads to a broad scattering intensity distribution in the WAXS range indicating a close to isotropic state. In temperature region **B**, the transition from the liquid−crystalline into the liquid−isotropic phase occurs. With the melting of the amphiphiles, the lamella architecture changes as well as indicated by the shift of the Bragg reflexes in the direction of higher q values. The ML thickness decreases and reaches a minimum of $d = 30.2 \pm 0.5$ Å at $T = 343.5 \pm 1$ K (Figure 6ii) and remains constant up to T = 384 K. The c_p maximum in region **B** at 344.5 ± 1 K (Figure 5i) is located 4 ± 1 K below the melting point of neat crystalline DHP (T_M(DHP) = 348.5

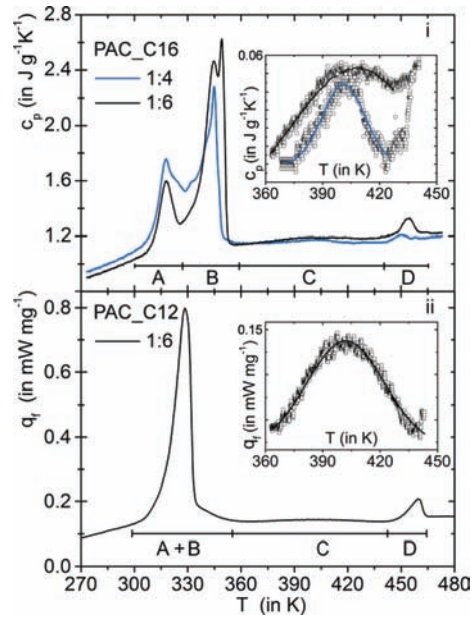

Figure 5. (i) Specific heat (c_p) of PAC_C16 with 1:4 (blue line) and 1:6 (black line) as function of temperature. Four different transitions can be observed: **A**, decrease of long-range order; **B**, melting of amphiphiles; **C**, spin-crossover and structure change; **D**, depolymerization. (ii): Heat flow (q_f) of PAC_C12_1:6 (black line) as function of temperature. **A**−**B**, transition from amphiphilic double- to monolayer and melting of the amphiphiles; **C**, spin-crossover; **D**, depolymerization. Insets: The SCO range, **C**, showing that in PACs the temperature range of SCO (region **C**) and of disassembly (region **D**) can partially overlap, as in PAC_C16_1:6, followed by an irreversible SCO. Otherwise, the regions overlap only slightly as in PAC_C16_1:4, where the SCO is partly reversible or they do not overlap and the SCO is totally reversible as in PAC_C12_1:6. Measurements are carried out using a differential scanning calorimeter with a measurement error of $T \pm 0.6$ K and $c_p \pm 0.008$ J g^{-1} K^{-1}.

(31) Bodenthin, Y.; Pietsch, U.; Grenzer, J.; Geue, T.; Möhwald, H.; Kurth, D. G. *J. Phys. Chem. B* **2005**, *109*, 12795–12799.

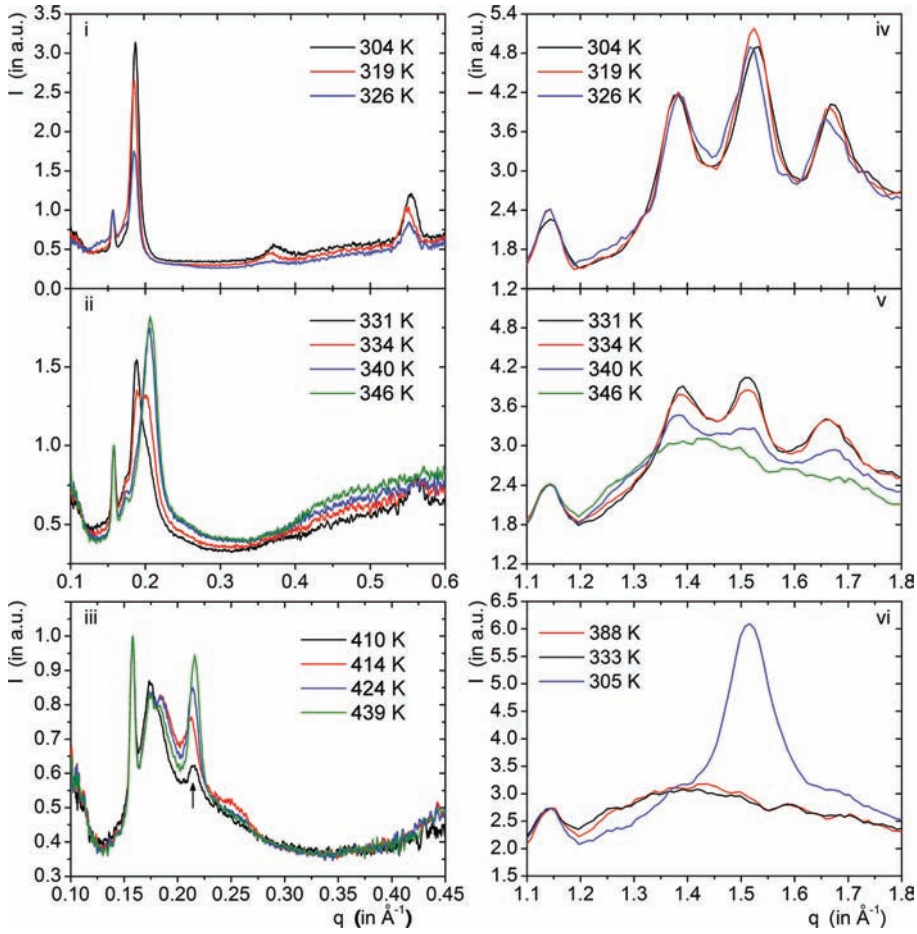

Figure 6. Scattering intensity (I) of Fe−PAC1_C16_[R] with [R] = 1:6 as function of the transfer momentum (q). SAXS intensities (left) and WAXS intensities (right) at increasing temperatures (T). (i, iv) From 304−326 K related to transition region **A** in Figure 4; (ii, v) from 331−346 K related to region **B**; and (iii) from 410−439 K related to region **C**. (vi) WAXS intensities during back to room temperature after heating up to 390 K. The measurement error is ±0.005 Å^{-1} for q and ±1 K for the temperature.

± 1 K).[32] In the first heating scan of PAC_C16_1:6, we note a third c_p maximum at T = 348.8 ± 1 K (Figure 5), which is exactly the value of the DHP melting point. This peak vanishes in subsequent heating cycles. Apparently, the amphiphilic matrix is composed of DHP electrostatically associated with MEPE and of free uncoordinated DHP. After the second heating cycle, the PAC is composed of a uniform liquid−crystalline phase.

The reason for this behavior may be associated with the spatial requirements of the components. Based on the measured dimensions of the methylene subcell (*vide supra*), the projected area of six amphiphiles in the plane perpendicular to the alkyl chains amounts to 226 Å^2 (Table 1). In the solid state, the corresponding area of a MEPE repeat unit based on the previously published data amounts to approximately 120 Å^2.[33] Obviously, there is a mismatch between the spatial requirement of the amphiphiles and the MEPE repeat unit in the case a of monolayer architecture. As a result, the amphiphilic matrix may initially be composed of two domains, associated and free DHP. While we are currently not able to differentiate these domains by spectroscopic or scattering methods, this hypothesis finds support in the transition at T = 348.8 ± 1 K (Figure 5). However, we cannot derive at this point a generic rule concerning the composition and the resulting PAC architecture.

PAC_C16_1:6 does not show a SCO in the temperature range from 273 to 373 K. Heat flow measurements show that the transitions **A**−**B** are fully reproducible (Figure 5 and S4 of the Supporting Information). We assume that the structure and phase transitions of the amphiphiles primarily contribute to the enthalpy in this range, which is given by the area under the peak. In the following, the total enthalpy (ΔH_T) for the transitions regions (**A**−**B**) in the temperature range 273−373 K are summarized. For the first heating cycle, ΔH_T is 81.4 ± 1 kJ mol^{-1}, which is considerably smaller the melting enthalpy of crystalline DHP (ΔH_M = 120.3 kJ mol^{-1}).[32] For the first cooling cycle, we find ΔH_T = −71.9 ± 1 kJ mol^{-1}. During cooling, the scattering peaks in the wide-angle region remain broad in the temperature range from 373 to 333 K (Figure 6vi). From 333 K onward, the scattering intensity increases, and below 308 K, a clear reflex at q = 1.53 Å^{-1} appears related to a simple hexagonal structure. This reassembly of DHP is reproducible even if the sample is heated above 373 K. For further heating and cooling cycles, $|\Delta H_T|$ remains constant (71.9 ± 1 kJ mol^{-1}). We assume that the enthalpy difference of ∼10 kJ mol^{-1} between the first and the second heating cycle is caused by the transition from a distorted hexagonal to a simple hexagonal packing motive. The absence of a second specific heat peak in region **B** after the first heating cycle supports our

(32) Thünemann, A. F.; Kurth, D. G.; Beinhoff, M.; Bienert, R.; Schulz, B. *Langmuir* **2006**, *22*, 5856–5861.
(33) Kolb, U.; Büscher, K.; Helm, C. A.; Lindner, A.; Thünemann, A. F.; Menzel, M.; Higuchi, M.; Kurth, D. G. *Proc. Natl. Acad. Sci. U.S.A.* **2006**, *103*, 10202–10206.

hypothesis that initially free uncoordinated DHP is present in the amphiphilic matrix.

By considering a SCO onset temperature (T_{oSCO}) of 410 K and an average SCO temperature of T_{aSCO} = 436 K for PAC_C16_1:6 (Table 3), the structure and phase transitions below 373 are not responsible for the SCO. However, Figure 5 shows two further c_p transitions **C** and **D**. For PAC_C16_1:6, the maximum of the transition in region **C** is at $T = 413 \pm 0.5$ K corresponding to T_{oSCO}. The calculated transition enthalpy and entropy are in agreement with literature values for LS to HS transitions in Fe^{2+} compounds and amount to $\Delta H_{SCO} = 7 \pm 1$ kJ mol^{-1} and $\Delta S_{SCO} = 17.8 \pm 1$ J mol^{-1} K^{-1}.[34,35] Therefore, we conclude that transition **C** is associated with the spin-crossover of PAC_C16_1:6. Figure 6iii shows that, at 410 ± 2 K, a new SAXS reflex appears (arrow) related to a lamella structure with a reduced thickness of $d = 29.3 \pm 0.5$ Å. The reflex intensity grows with increasing temperature and reaches a maximum at 439 ± 2 K. Upon further heating, the intensity decreases again.

Transition **D** above 439 K (Figure 4i) is possibly caused by disassembly of the MEPE or emergence of other defects in the Fe−MEPE chain. By thermogravimetric analysis, we can exclude decomposition or other chemical reactions. We note that redissolving and precipitating the sample fully recovers the original properties.[36] If the sample is heated up to region **D**, the SCO is irreversible. If the temperature range of SCO (region **C**) and disassembly (region **D**) partially overlap, as in PAC_C16_R1:6 (Figures 4i and 5i, inset), the SCO is irreversible. Otherwise, the SCO is partly reversible as in PAC_C16_1:4 (Figures 4i and 5i, inset).

The reference compound Ni−PAC_C16_1:6 does not show a SCO in the investigated temperature range but a constant magnetic moment of 3.0 ± 0.5 μB/Ni^{2+}. This value correlates fairly well with pure spin magnetism of Ni^{2+} in a octahedral coordination geometry (2.83 μB/Ni^{2+}).[37] In the same manner, Ni−PAC_C16_1:6 does reveal any phase transition in DSC from 373 to 443 K (region **C**). For Ni−PAC_C16_R1:6, transition **D** occurs at higher temperatures, which may be related to the higher binding constant of Ni and terpyridine compared to Fe.[38] As a result, disassembly of Ni−MEPE occurs at a higher temperature. We note that, besides these differences, the scattering data of Ni−PAC_C16_1:6 indicates the same structure changes in the amphiphilic matrix as the corresponding Fe−PAC.

The environment of the Fe^{2+} coordination center is explored by X-ray absorption fine structure (EXAFS) analysis. A representative EXAFS function of solid Fe−PAC is shown in the Supporting Information (Figure S5). For the fit of the data, a two-core approximation is used with two different Fe−N distances (r_1 and r_2). The axial bond length, r_1, amounts to 1.85 ± 0.02 Å, and the equatorial bond length, r_2, is 1.98 ± 0.02 Å. The occupation numbers are 2 for the axial positions and 4 for the equatorial positions in agreement with a pseudo-octahedral coordination geometry. This geometry around the Fe^{2+} ions is

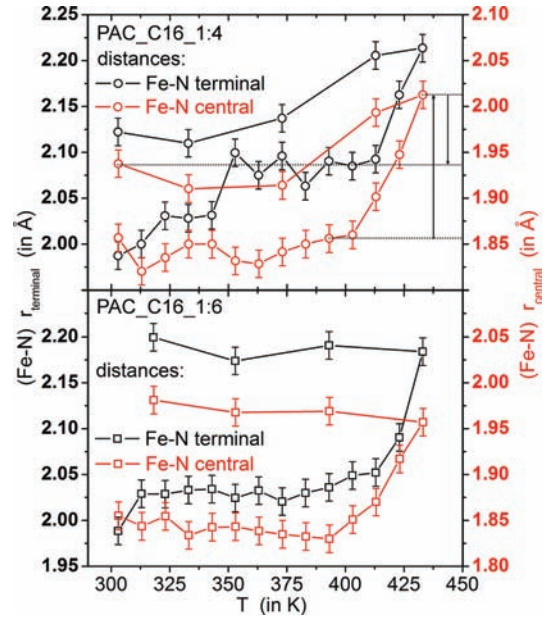

Figure 7. Fe^{2+} distances to the central nitrogen atoms of the terpyridine ligands (red line) and to the terminal nitrogen atoms (black line) as a function of temperature for PAC_C16_1:4 (top) and PAC_C16_1:6 (bottom) determined with EXAFS measurements. During heating, the average values of the Fe−N distances of both PAC increase by 0.12−0.16 Å. The temperature range correlates with the observed spin-crossover temperature. For PAC_C16_1:6, the reached Fe−N distances remain elongated after cooling (bottom), and for PAC_C16_1:4, the distances decrease as indicated through the dotted lines and the arrows (top). This result is in agreement with the magnetic measurements where the temperature dependent magnetic susceptibility shows a similar behavior.

generally observed with terpyridine (tpy) ligands[30] and is supposed for the entire heating cycle. The values mentioned above correspond fairly well with average Fe−N next-neighbor distances in the single crystal structure of the mononuclear $[Fe(tpy)_2]^{2+}$ complex.[39] These Fe−N distances are typical for a LS state. It should be noted that it is not possible to obtain a satisfactory fit with a single shell model, where all bond distances are equal (not shown). Upon heating, both Fe−N distances of PAC_C16_1:6, r_1 and r_2, increase on average by 0.16 ± 0.02 Å beginning at $T = 413$ K up to $T = 433$ K (Figure 7). This change in bond length is typical for a spin-crossover, as antibonding orbitals are occupied.[40] This result is the final proof for a spin-crossover in temperature region **C**. The enhanced Fe−N distances remain constant after cooling to room temperature, which is in agreement with an irreversible SCO.

Next, we discuss the structure and phase transitions of PAC_C12_1:6 and PAC_C16_1:4, which in contrast to PAC_C16_1:6, have a double layer architecture and a partly or totally reversible SCO. Not surprisingly, the melting temperature T_M of PAC_C12_1:6 is 326 ± 1 K about 20 K lower than for PAC_C16_1:6. The melting temperature of the pure amphiphile dodecylphosphate (DDP) is $T_M = 335.4 \pm 1$ K and again almost 10 K higher than the corresponding PAC. The melting enthalpy of DDP amounts to $\Delta H_M = 90.4$ kJ mol^{-1}.[32] The transition enthalpy ΔH_T of PAC_C12_1:6 is 48.2 kJ mol^{-1} in the range from $T = 298-358$ K (Figure 5ii). In the scattering data, we observe a new phenomenon in this temperature range. As the amphiphiles melt, we also observe a transition from the double- to the monolayer architecture of the amphiphilic matrix. At room

(34) Papánková, B.; Vrbová, M.; Boca, R.; Simon, P.; Falk, K.; Miehe, G.; Fuess, H. *J. Therm. Anal. Cal.* **2002**, *67*, 721–731.
(35) König, E. *Structure and Bonding*; Springer Verlag: Berlin, Germany, 1999; Vol. 76.
(36) Bodenthin, Y.; Schwarz, G.; Tomkowicz, Z.; Lommel, M.; Geue, T.; Haase, W.; Möhwald, H.; Pietsch, U.; Kurth, D. G. *Coord. Chem. Rev.* **2009**, *253*, 2414–2422.
(37) Lueken, H. *Magnetochemie: Eine Einführung in Theorie und Anwendung*; 1st ed.; Teubner Verlag: Stuttgart, Germany, 1999.
(38) Holyer, R. H.; Hubbard, I. C. D.; Kettle, S. F. A.; Wilkins, R. G. *Inorg. Chem.* **1966**, *5*, 622–625.
(39) Baker, A. T.; Goodwin, H. A. *Aust. J. Chem.* **1985**, *38*, 207–214.
(40) Sato, O.; Tao, J.; Zhang, Y. Z. *Angew. Chem.* **2007**, *119*, 2200–2236.

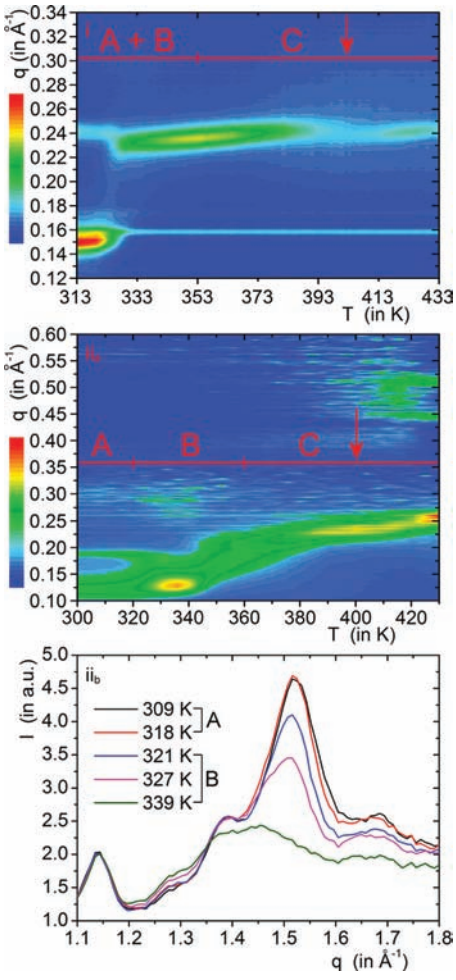

Figure 8. Time resolved energy-dispersive SAXS (EDR) pattern of PAC_C12_1:6 (top) and PAC_C16_1:4 (middle) showing the transfer momentum (q) as a function of temperature (T). The scattering intensity is color-coded as indicated on the left side, with dark blue for the lowest and red for the highest intensity. The temperature ranges **A**−**C** (above the red line) indicate the transitions measured with differential scanning calorimetry (Figure 4). (Top) The peak at $q = 0.16$ Å^{-1} (light blue) persistent over the whole temperature range corresponds to the iron K_α fluorescence at 6.4 keV. At 313 K, one can see the first order reflexes of the amphiphilic double and monolayer of PAC at $q = 0.15$ and 0.24 Å^{-1}. In the transition regions **A**−**B**, the amphiphiles melt between 313 and 333 K and the double layer change into monolayer. Between 313 and 323 K, the thickness of the monolayer increases slightly from 26.1 to 27.3 Å indicated through a peak shift to lower q. With further heating, the layer thickness decreases again to the initial value. The spin-crossover start (onset) is indicated by an arrow. During the SCO, a new structure arises supporting the low-spin to high-spin transition. (Middle) In the temperature range above 319 ± 2 K (region **B**), all amphiphile double layer transit into monolayer indicated by the shift of the double layer peak at $q = 0.12$ to the monolayer peak at $q = 0.19$. Above 344 K, the layer transition has finished, and the amphiphiles are in a liquid isotropic phase. Heating further into temperature region **C** changes the monolayer thickness from $d = 33.3$ Å to $d = 29.9$ Å. At 401 K, a new structure arises with a first and second order Bragg reflex at $q = 0.26$ and 0.52 Å^{-1} (arrow). This structure change is reversible as long as the temperature does not exceed 440 K or region **C**, respectively. Along with the new structure formation starts the spin-crossover. (Bottom) WAXS intensity (I) of PAC_C16_1:4 as function of q at different temperatures in the regions **A**−**B** indicating that the melting of the amphiphiles begins with temperature region **B**.

temperature, the DL and ML architecture coexist in the sample with a ratio of nearly 3:1 (Table 2). The first order ML and DL Bragg reflex is at $q = 0.241$ and 0.148 Å^{-1}, respectively, or $d = 26.1$ and 42.5 Å (Table 2 and Figure 8i). Between 323 and 333 K the DL architecture changes into the ML structure as demonstrated by the disappearance of the DL reflex and the increase of the ML reflex (Figure 8i). At 393 ± 2 K, the first order ML reflex vanishes and reappears again at 403 K slightly shifted to $q = 0.235 \pm 0.002$ Å^{-1} corresponding to a monolayer periodicity of $d = 26.7 \pm 0.3$ Å^{-1}. This temperature ($T = 403$ K, Figure 8i, arrow) corresponds to the maximum of the transition region **C** (from 366 to 438 K). By heating the sample above the upper limit of **C** into region **D**, the SCO becomes partly or completely irreversible. Simultaneously, the reflex of the ML structure vanishes irreversibly. If the sample is cooled before region **D** is reached, the hexagonal distorted packing of the amphiphiles fully recovers at room temperature with a periodicity of the ML structure of $d = 26.1 \pm 0.5$ Å.

The melting temperature $T_M = 344.5 \pm 1$ K of PAC_C16_1:4 is within 4 ± 1 K again lower than that of the pure amphiphile. During the first heating from 273 to 383 K, the enthalpy ΔH_T amounts to 79.7 ± 1 kJ mol^{-1}. For successive heating and cooling cycles, the transition enthalpy amounts to $\Delta H_T = 54.9 \pm 1$ kJ mol^{-1}. Scattering measurements show that the distorted hexagonal packing of the amphiphiles vanishes above 319 ± 2 K. In addition, we observe a transition of the double layer structure to a monolayer structure (Figure 8, middle) as indicated by the changes in the intensity of the corresponding scattering peaks at $q = 0.121$ (DL) and $q = 0.189$ (ML). Above 344 K, the layer transition is complete, and the amphiphiles are in a liquid isotropic phase as indicated by the absence of scattering intensity in the wide-angle region. Further heating into temperature region **C** changes the ML thickness from $d = 33.3 \pm 0.5$ Å to $d = 29.9 \pm 0.5$ Å. At 401 K, a new structure arises with a first and second order Bragg reflex at $q = 0.26 \pm 0.03$ and 0.52 ± 0.03 Å^{-1} (arrow in Figure 8, middle). This structure change is reversible as long as the temperature does not exceed 440 K or region **C**, respectively. Heating further into region **D** and cooling down to room temperature, this structure is maintained; however, the ML-structure is recovered if the sample is annealed at ∼344 K. As mentioned above, the SCO (Figure 4i) occurs in temperature range **C** (Figure 5i), which is also accompanied by an increase of the Fe−N distances (Figure 7, top). The transition enthalpy ΔH_{SCO} of 4.5 ± 1 kJ mol^{-1} and the transition entropy ΔS_{SCO} of 13.2 ± 1 J mol^{-1} K^{-1} indicate an incomplete SCO of PAC_C16_1:4.

Finally, we address the results for the metallo-supramolecular compound assembled from flexible ligand (reference) and Fe^{2+} metal ions. As reported previously, the short, flexible ligand results in low-molecular ringlike structures.[21,22] Therefore, we refer to this kind of assembly as metallo-supramolecular oligomer (MSO) and oligomer−amphiphile complex (OAC). SAXS measurements of the corresponding OAC_C16_1:4 and OAC_C16_1:6 reveal the same lamella architecture as for PAC_C16_1:4 and PAC_C16_1:6 (Figure 9i). Just as for PAC, DHP double layers are the dominating architecture in OAC_C16_1:4 and interdigitating DHP monolayers in OAC_C16_1:6 (Table 2). The heat flow measurement of OAC_C16_1:6 in the temperature range from 273 to 393 K is similar to that of PAC_C16_1:6. Transition **A** from 300 to 327 K (Figure 9ii) correlates to the decrease of the long-range order between the lamella structures. Above this temperature in region **B**, the melting of the amphiphiles starts accompanied by a decrease of the WAXS intensity (not shown) and ends with the q_f maximum at 342.4 ± 1 K. The melting of the OAC is 6.1 ± 1 K below the melting point of neat crystalline DHP (348.5 ± 1 K). We note that transition region **D** attributed to disassembly or defects in MEPE is not detected in the range from 273 to

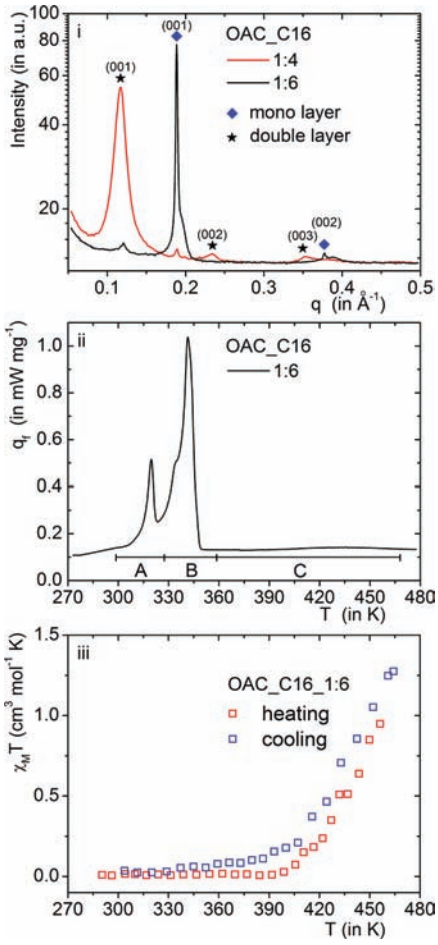

Figure 9. (i) Scattering intensity (I) as a function of the transfer momentum (q) of OAC_C16 with R = 1:4 (red line) and 1:6 (black line). For R = 1:4, the double layer motif of the amphiphiles dominates, and for R = 1:6, the monolayer motif dominates. (ii) Heat flow (q_f) for OAC_C16_1:6 (black line) as function of temperature. Three different transitions can be observed in the regions **A**−**C**: **A** is related to the decrease of long-range order between the lamella structures; **B** corresponds to the melting of the linked amphiphiles; and **C** corresponds to the spin-crossover temperature. (iii) Product of magnetic susceptibility (χ_M) and the temperature (T) as a function of temperature (T) of OAC_C16_1:6 during a first heating (red squares) and cooling (blue squares) cycle. The data taken with a Faraday balance reveals an increase of $\chi_M T$ during the heating cycle and a decrease during the cooling cycle. This corresponds to a reversible but partial spin-crossover between a diamagnetic low-spin state and a paramagnetic high-spin state of the Fe^{2+} ion of the OAC.

483 K. We assume that the higher flexibility and the shorter chains of the MEPEs are reasons for the absence. A broad SCO range is observed in the range from 373 to 467 K (region **C**). At 467 K, the magnetic susceptibility reaches a value of 1.36 cm^3 mol^{-1} K. At this point, only 62% of Fe^{2+} ions are in the HS state. We did not measure at higher temperatures due to the thermal decomposition above 473 K. In summary, OAC_C16_1:6 shows a partial but totally reversible SCO. The architecture of the assembly is apparently dictated by the amphiphile component.

In summary, we conclude that, at temperatures above 400 K for all PACs with R = 1:4 and 1:6, a new structure is formed associated with a spin-crossover, which is indicated by the magnetic and DSC measurements. This temperature is above the melting temperature of the amphiphilic phase in PAC as indicated by the loss of scattering intensity in the wide-angle region. The amphiphilic double layer architecture changes to an interdigitated monolayer architecture just before (Figure 5 region **A**) or during melting of the amphiphiles (region **B**). If the temperature region of the SCO (**C**) is well separated from the disassembly temperature (region **D**), the transition is partially or totally reversible, otherwise it is irreversible. We note that the enthalpies of the SOC are too low for an ordinary entropy-driven spin transition, so we conclude that the contemporaneous structure change contributes to and enables the SCO. Ni−PAC shows the same structural changes; however, we do not observe a SCO or the corresponding transition in DSC. With a flexible ligand, we observe a partial but reversible SCO.

Conclusion

Sequential self-assembly of transition metal ions with rigid ditopic bisterpyridines and dialkyl phosphates results in polyelectrolyte amphiphile complexes (PAC) with a lamellar architecture. The final architecture of PACs depends in a nontrivial way on the metal ion to amphiphile ratio. The amphiphiles form either interdigitated monolayers or double layers with hexagonal or distorted hexagonal packed alkyl chains. The interstitial space between the amphiphile layers is filled with MEPE, which is formed by metal ion induced self-assembly of the transition metal ion and the ligands. The coordination environment of the metal centers in the MEPE chain is pseudo-octahedral with two different Fe−N distances, which is expected for bisterpyridine complexes. At room temperature, only a minor fraction of Fe^{2+} ions in PAC (10−25%) are in the high-spin (HS) state. Heating the PAC results in a spin-crossover (SCO) in a temperature range from 360 to 460 K depending on the PAC architecture. As the number of amphiphiles per metal ion is increased in the sequence R = 1:2, 1:4, and 1:6, the temperature of the SCO is shifted to higher values. The amphiphile chain length does not have a significant impact on the SCO temperature. For R = 1:2, the melting of the amphiphilic phase and the SCO occur in adjacent almost overlapping temperature ranges. We propose that the melting of the amphiphilic phase causes sufficient strain to distort the MEPE chain thus inducing a complete but irreversible SCO. Only for the PAC_C16_1:2 we unambiguously determine the architecture from scattering data. The amphiphiles pack in regular hexagonal lattice and an interdigitated monolayer architecture. The weak scattering signals of the other two PACs indicate the absence of long-range order and therefore do not allow unambiguous conclusion about the structure. In contrast, for PAC with R = 1:4 and R = 1:6, the melting of the amphiphilic matrix and the SCO occur in well-separated temperature range. The enthalpies of the SCO are too small for simple temperature-induced spin transition. While the temperature is above the melting of the amphiphilic phase, we do observe that the SCO is accompanied by a structure change. Apparently, the amphiphilic phase does assist or enable the SCO. During the SCO the Fe−N distances increase by about 0.16 Å, which is in agreement with results from single crystal studies of mononuclear terpyridine.[40] If the temperature range of the SCO (region **C**) is well separated from the temperature of disassembly (region **D**), the SCO is reversible. If the two temperature regions overlap, the SCO is irreversible. Apparently, the defects created in the MEPE chain do not heal upon cooling; however, dissolving and reprecipitating the sample recovers the original structure and properties. We note that the SCO of the presented PACs is partially or completely reversible if the amphiphilic matrix has the double layer architecture. If the amphiphiles are organized in the monolayer architecture, the SCO is irreversible. Ni−PACs used as reference compounds have the same structure as the equivalent Fe−PACs and follow the same structure changes during heating but do not show a SCO. For the first time, the temperature dependent magnetic

properties and the structures of oligomer amphiphilic complexes are characterized. Thereby OAC_C16_1:6 shows a partial but totally reversible SCO. The architecture of these assemblies is apparently dictated by the amphiphile component and corresponds to the layer motives of PAC. In summary, we document that the structure and the magnetic response function of PACs can be tailored through the design of the ligand and the composition. In the future, it will be of interest to study how we can improve the magnetic response function in PACs including the temperature range of the SCO and the reversibility through the choice of ligands, metal ions, and self-assembly conditions as well through matrix variations.

Experimental Section

The ligands 1,4-bis(2,2′:6′2″-terpyridine-4′-yl) benzene (**L1**)[41] and 1,3-bis[4′-oxa(2,2′:6′,2″-terpyridinyl)]propane (**L2**)[42−44] were synthesized and characterized according to literature procedures. Chemicals were purchased from Aldrich and were used without further purification. The Fe−MEPE synthesis with a metal ion to ligand ratio of 1:1 considered the instructions in literature. A representative PAC synthesis with a 1:6 stoichiometry of MEPE repeat unit to DHP was as follows: 458.33 mg (0.84 mmol) of dihexadecyl phosphate (DHP) was added to 100 mg (0.14 mmol) under high vacuum-dried Fe−MEPE1, and the solids were dispersed in 60 mL of $CHCl_3$. After 24 h stirring at room temperature, the solvent of the clear dark blue solution was evaporated under ambient pressure, and the dark blue solid was dried under vacuum. The magnetic properties were probed by using a DC-SQUID magnetometer from Quantum Design and a Faraday balance with maximum upper temperatures of 400 and 473 K, respectively. The SQUID provides a sensitivity of e10^{-7} emu, while for high temperatures, we probed the sample by a Faraday balance under He gas atmosphere with a sensitivity of 10^{-5} emu (external field $B = 1.2$ T).[45] Due to the lower sensitivity, we took sample masses above 25 mg. For corrections of the magnetic background, we measured pure ligand and amphiphil samples. To verify the experimental values of the magnetic susceptibility, we measured $\chi_M T$ as a function of temperature from 300 to 4 K using a SQUID magnetometer after heating the sample above the SCO temperature in the Faraday balance to switch the Fe^{2+} ions into the high-spin state. The SQUID measured $\chi_M T$ data were fitted to the Curie−Weiss law to verify the experimental data mathematical, for example, in Figure S3 of the Supporting Information for Fe−PAC1_C16_1:6. We used a heating rate of 2 K min^{-1} for the magnetic measurements as well as for the structural investigations. DSC and TGA measurements were performed under N_2 atmosphere with a heating rate of 2 K min^{-1} on a DSC 204 F1 Phoenix and a TG 209 F1, respectively. For estimation of the heat capacity (c_p), three records were taken as a function of temperature: first, the heat flow of the empty aluminum sample holder; second, the heat flow of the sample in the holder; and third, the heat flow of the reference material, sapphire. These heat flows were processed by a procedure summarized through Höhne et al. to obtain the heat capacity of the sample.[34,46] The error for comparison temperatures of different experiments is estimated to be ±5 K. Small-angle X-ray scattering was performed at the energy dispersive reflectometer at the BESSY II synchrotron.[47] Here, the hard X-ray decay of a bending magnet is used for scattering providing X-rays in an energy range of 5−25 keV. SAXS patterns are collected as a function of temperature using two energy-dispersive detectors with an energy resolution of $\Delta E/E = 10^{-2}$. To enhance the accessible q range, the detectors are equipped at two fixed exit angles of $2\theta = 2.79°$ and $2\theta = 5.78°$ with respect to the incident beam. This geometry provides sufficient counting statistics in a q range of 0.05 $Å^{-1} \le q \le 0.80$ $Å^{-1}$ and a time resolution of 60 s per spectrum.[48] Extended X-ray absorption fine structure (EXAFS) experiments were undertaken at the KMC 2 beamline at BESSY II, using the fluorescence yield $I_{fluo}(E) \sim \mu(E)$ of the Fe^{2+} ions, where $\mu(E)$ represents the absorption.[49] To explore the data, we used a simplex fitting algorithm to the EXAFS standard formula $\chi_{sim} = \Sigma_i(N_i/kr^2_i)\exp(-2\sigma^2_i k^2)\exp(-2r_i/\lambda(k)) \times |f_i(k, r_i)|\sin(2kR_i + \Phi(k, r_i))$ minimizing the residual $S = (\Sigma(\chi_{exp}(k) - \chi_{sim}(k))^2/\Sigma\chi_{exp}{}^2(k))^{0.5}$. k represents the reduced wavenumber $k = \hbar^{-1}(2\ \mu_e(E - E_0))^{0.5}$, E the photon energy, E_0 the iron absorption edge, N_i the occupation number, σ^2 the Debye−Waller factor, and r_i the radius of the shell. The amplitude $f(k, r)$ and phase $\Phi(k, r)$ were calculated with the ab initio FEFF6 calculation.[50] In order to avoid the "multiple solution trap",[51] the Fe−N distances were restrained to vary in an interval of ±0.2 Å. The calculations presume a pseudo-octahedral coordination geometry over the whole temperature range and Fe−N changes less than 0.25 Å. Small-angle neutron scattering (SANS) measurements were carried out at the SANS II Beamline[52] at the Paul Scherer Institute (Switzerland), with three different wavelength $\lambda_{1,2} = 6.73$ Å and $\lambda_3 = 19.6$ Å and three different sample to detector distances of $SDD_1 = 1.2$ m, $SDD_2 = 5$ m and $SDD_3 = 6$ m, providing sufficient counting statistics in a q range of $10^{-4} \le q \le 0.4$ Å. Spinpolarized SANS was measured at the SANS I beamline[53] at PSI. The magnetic field of 11 T was applied to the sample by an electromagnet oriented parallel or antiparallel to the spin polarization.

Acknowledgment. This work was supported by Deutsche Forschungsgemeinschaft as part of the priority program 1137 "Molecular Magnetism". This work is partly based on experiments performed at the Swiss spallation neutron source SINQ, Paul Scherrer Institut, Villigen, Switzerland and on the BESSY II synchrotron Berlin, Germany. The authors thank Helmuth Möhwald for valuable discussions and Martin Lommel for the experimental support.

Supporting Information Available: SAXS data of PAC_Cx_1:2 with $x = 12$, 14, and 16 (S1); SAXS data of PAC_C16_1:6 with different metal ions (Fe^{2+}, Co^{2+}, and Ni^{2+}) (S2); $\chi^*T(T)$ curve for PAC_C16_1:6 measured with SQUID and Faraday Balance and fitted to the Curie−Weiss law (S3); heat flow (q_f) of PAC_C16_1:6 during three consecutively heating and cooling cycles (S4); and a representative EXAFS function of PAC_C16_1:4 at room temperature (S5). This material is available free of charge via the Internet at http://pubs.acs.org.

JA108416A

(41) Constable, E. C.; Cargill Thompson, A. M. W. *J. Chem. Soc., Dalton Trans.* **1992**, 3467–3475.
(42) Schubert, U. S.; Eschbaumer, C.; Hien, O.; Andres, P. R. *Tetrahedron Lett.* **2001**, *42*, 4705–4707.
(43) Lehmann, P.; Symietz, C.; Brezesinski, G.; Krass, H.; Kurth, D. G. *Langmuir* **2005**, *21*, 5901–5906.
(44) Maanpää, L.; Luzet, V.; Guillaume, G.; Taherpour, S.; Maki, E.; Mikkola, S. *New J. Chem.* **2009**, *33*, 1853–1858.
(45) Merz, L.; Haase, W. *J. Chem. Soc., Dalton Trans.* **1980**, 875–879.
(46) Höhne, G.; Hemminger, W.; Flammersheim, H. J. *Differential Scanning Calorimetry*; Springer Verlag: Berlin, Germany, 1996.
(47) Pietsch, U.; Grenzer, J.; Geue, T.; Neissendorfer, F.; Brezsesinski, G.; Symietz, C.; Möhwald, H.; Gudat, W. *Nucl. Instrum. Methods Phys. Res., Sect. A* **2001**, *467*, 1077–1080.
(48) Bodenthin, Y.; Grenzer, J.; Lauter, R.; Pietsch, U.; Lehmann, P.; Kurth, D. G.; Möhwald, H. *J. Synchrotron Rad.* **2002**, *9*, 206–209.
(49) Erko, A.; Packe, I.; Gudat, W.; Abrosimov, N.; Firsov, A. *SPIE* **2000**, *4145*, 122–128.
(50) Rehr, J. J.; Albers, R. C.; Zabinsky, S. I. *Phys. Rev. Lett.* **1992**, *69*, 3397–3400.
(51) Michalowicz, A.; Vlaic, G. *J. Synchrotron Rad.* **1998**, *5*, 1317–1320.
(52) Strunz, P.; Mortensen, K.; Janssen, S. *Phys. B (Amsterdam, Neth.)* **2004**, *350*, E783−E786.
(53) Aswal, V. K.; van den Brandt, B.; Hautle, P.; Kohlbrecher, J.; Konter, J. A.; Michels, A.; Piegsa, F. M.; Stahn, J.; Van Petegem, S.; Zimmer, O. *Nucl. Instrum. Methods Phys. Res., Sect. A* **2008**, *586*, 86–89.